

MIT Open Access Articles

TOI 540 b: A Planet Smaller than Earth Orbiting a Nearby Rapidly Rotating Low-mass Star

The MIT Faculty has made this article openly available. **Please share** how this access benefits you. Your story matters.

As Published: 10.3847/1538-3881/ABBD91

Publisher: American Astronomical Society

Persistent URL: <https://hdl.handle.net/1721.1/134080>

Version: Final published version: final published article, as it appeared in a journal, conference proceedings, or other formally published context

Terms of Use: Article is made available in accordance with the publisher's policy and may be subject to US copyright law. Please refer to the publisher's site for terms of use.





TOI 540 b: A Planet Smaller than Earth Orbiting a Nearby Rapidly Rotating Low-mass Star

Kristo Ment¹ , Jonathan Irwin¹, David Charbonneau¹ , Jennifer G. Winters¹ , Amber Medina¹ , Ryan Cloutier¹ , Matías R. Díaz² , James S. Jenkins^{2,3} , Carl Ziegler⁴ , Nicholas Law⁵ , Andrew W. Mann⁵ , George Ricker^{6,7} , Roland Vanderspek^{6,7} , David W. Latham¹ , Sara Seager^{6,7,8,9}, Joshua N. Winn¹⁰ , Jon M. Jenkins¹¹ , Robert F. Goike⁷ , Alan M. Levine⁷ , Bárbara Rojas-Ayala¹² , Pamela Rowden¹³ , Eric B. Ting¹¹ , and Joseph D. Twicken^{11,14}

¹Center for Astrophysics, Harvard & Smithsonian, 60 Garden Street, Cambridge, MA 02138, USA; kristo.ment@cfa.harvard.edu

²Departamento de Astronomía, Universidad de Chile, Camino El Observatorio 1515, Las Condes, Santiago, Chile

³Centro de Astrofísica y Tecnologías Afines (CATA), Casilla 36-D, Santiago, Chile

⁴Dunlap Institute for Astronomy and Astrophysics, University of Toronto, 50 St. George Street, Toronto, Ontario M5S 3H4, Canada

⁵Department of Physics and Astronomy, The University of North Carolina at Chapel Hill, Chapel Hill, NC 27599-3255, USA

⁶Department of Earth, Atmospheric and Planetary Sciences, Massachusetts Institute of Technology, Cambridge, MA 02139, USA

⁷Kavli Institute for Astrophysics and Space Research, Massachusetts Institute of Technology, Cambridge, MA 02139, USA

⁸Department of Aeronautics and Astronautics, MIT, 77 Massachusetts Avenue, Cambridge, MA 02139, USA

⁹Department of Physics, Massachusetts Institute of Technology, Cambridge, MA 02139, USA

¹⁰Department of Astrophysical Sciences, Princeton University, Princeton, NJ 08544, USA

¹¹NASA Ames Research Center, Moffett Field, CA 94035, USA

¹²Instituto de Alta Investigación, Universidad de Tarapacá, Casilla 7D, Arica, Chile

¹³School of Physical Sciences, The Open University, Milton Keynes MK7 6AA, UK

¹⁴SETI Institute, Mountain View, CA 94043, USA

Received 2020 July 16; revised 2020 September 24; accepted 2020 September 25; published 2020 December 11

Abstract

We present the discovery of TOI 540 b, a hot planet slightly smaller than Earth orbiting the low-mass star 2MASS J05051443-4756154. The planet has an orbital period of $P = 1.239149$ days (± 170 ms) and a radius of $r = 0.903 \pm 0.052 R_{\oplus}$, and is likely terrestrial based on the observed mass–radius distribution of small exoplanets at similar insolation. The star is 14.008 pc away and we estimate its mass and radius to be $M = 0.159 \pm 0.014 M_{\odot}$ and $R = 0.1895 \pm 0.0079 R_{\odot}$, respectively. The star is distinctive in its very short rotational period of $P_{\text{rot}} = 17.4264 \pm 0.0094$ hr and correspondingly small Rossby number of 0.007 as well as its high X-ray-to-bolometric luminosity ratio of $L_X/L_{\text{bol}} = 0.0028$ based on a serendipitous XMM-Newton detection during a slew operation. This is consistent with the X-ray emission being observed at a maximum value of $L_X/L_{\text{bol}} \simeq 10^{-3}$ as predicted for the most rapidly rotating M dwarfs. TOI 540 b may be an alluring target to study atmospheric erosion due to the strong stellar X-ray emission. It is also among the most accessible targets for transmission and emission spectroscopy and eclipse photometry with the James Webb Space Telescope, and may permit Doppler tomography with high-resolution spectroscopy during transit. This discovery is based on precise photometric data from the Transiting Exoplanet Survey Satellite and ground-based follow-up observations by the MEarth team.

Unified Astronomy Thesaurus concepts: [Transit photometry \(1709\)](#); [Exoplanets \(498\)](#); [Extrasolar rocky planets \(511\)](#); [Stellar rotation \(1629\)](#)

Supporting material: data behind figures, machine-readable table

1. Introduction

Obtaining a representative sample of rotation periods in planet-hosting M dwarfs is important due to the established link between rotation rate and stellar activity. Stars exhibit continual angular momentum loss due to magnetic braking, which subsequently decreases the strength of the stellar magnetic dynamo, leading to a decrease in activity (Skumanich 1972). Consequently, rapidly rotating stars tend to have higher levels of coronal X-ray emission (Wright et al. 2018). Elevated X-ray and UV emission are known tracers of increased magnetic activity (Gronoff et al. 2020) and will have profound consequences on the atmospheric mass loss and potential habitability of any terrestrial planets in the system (e.g., Garcia-Sage et al. 2017).

The vast majority of recent discoveries of terrestrial planets orbiting M dwarfs are in systems with relatively inactive host stars, characterized by stellar rotation periods longer than 100 days. Rapidly rotating stars present observational challenges for planet detection. Rotational broadening of spectral lines

significantly degrades in radial velocity (RV) precision, and irregularities of emitted flux from starspots and faculae that are rapidly shifting in and out of view across the stellar surface can imprint complicated modulations in the star’s observed flux, hampering transit detection. In addition, rapid rotation in M dwarfs also correlates with more frequent flare emission (Davenport 2016 and references therein), further contaminating the light curve. In particular, the current sample of terrestrial planet hosts within 15 pc of the Sun includes no red dwarfs with rotation periods less than a day, and only one ultracool dwarf with a rotation period below 10 days, TRAPPIST-1, which has an estimated $P_{\text{rot}} = 1.40 \pm 0.05$ days (Gillon et al. 2016) or $P_{\text{rot}} = 3.30 \pm 0.14$ days (Luger et al. 2017).

Transiting planets with radii around or less than $1 R_{\oplus}$ are of special interest because they are likely to be terrestrial even in the absence of mass constraints from precise RV or transit-timing variation (TTV) data. Weiss & Marcy (2014) and Rogers (2015) identified two distinct regimes in the mass–radius relation for small exoplanets: planets below a threshold

radius of $1.5 R_{\oplus}$ tend to have bulk densities consistent with a rocky composition whereas those above that threshold possess a large fraction of volatiles by volume. These results were based on numerous RV studies that had obtained masses for small transiting planets around G and K dwarfs such as Kepler-10 (Batalha et al. 2011), Kepler-78 (Howard et al. 2013; Pepe et al. 2013), and Kepler-93 (Dressing et al. 2015). Recent RV measurements have established rocky bulk composition for many small planets orbiting M dwarfs as well, including L 98-59 (Cloutier et al. 2019), LHS 1140 (Ment et al. 2019), LTT 3780 (Cloutier et al. 2020a), and TRAPPIST-1 (Grimm et al. 2018). Consistent with the interpretation of two distinct planet populations, Fulton et al. (2017) noticed a deficit of planets with radii $1.5\text{--}2 R_{\oplus}$ (a radius valley). The radius valley likely arises as a result of photoevaporation (Lopez & Fortney 2013; Owen & Wu 2013, 2017; Lopez & Rice 2018), core-powered mass loss (Ginzburg et al. 2018), or formation in a gas-poor environment (Lee et al. 2014; Lopez & Rice 2018). Its existence was demonstrated specifically for K and M dwarfs by Cloutier & Menou (2020) using K2 photometry.

Upcoming exo-atmospheric studies with state-of-the-art instruments such as the James Webb Space Telescope (JWST) and ground-based 30 m telescopes will primarily focus on the planets orbiting M dwarfs closest to the solar system. This is due to photon statistics as well as the relative size of the planet compared to the star that make both transmission and emission spectroscopy tractable (Morley et al. 2017). There are currently (as of 2020 April) only 10 stars within 15 pc of the Sun that are known to host transiting planets: the M dwarfs LTT 1445 A (Winters et al. 2019), GJ 357 (Luque et al. 2019), GJ 436 (Butler et al. 2004; Gillon et al. 2007), L 98-59 (Kostov et al. 2019), TRAPPIST-1 (Gillon et al. 2016, 2017b), GJ 1132 (Berta-Thompson et al. 2015; Bonfils et al. 2018), GJ 1214 (Charbonneau et al. 2009), LHS 3844 (Vanderspek et al. 2019), LHS 1140 (Dittmann et al. 2017; Ment et al. 2019), and the K dwarfs 55 Cnc A (McArthur et al. 2004; Winn et al. 2011) and HD 219134 (Motalebi et al. 2015; Vogt et al. 2015; Gillon et al. 2017a); only two of those systems (L 98-59 and TRAPPIST-1) are known to host planets smaller than $1 R_{\oplus}$. Four of the planetary systems described above (LTT 1445, GJ 357, L 98-59, and LHS 3844) were discovered with the Transiting Exoplanet Survey Satellite (TESS; Ricker et al. 2015).

This article presents the discovery of TESS Object of Interest (TOI) 540 b, a $0.9 R_{\oplus}$ planet on a 1.24 day orbit discovered by TESS. With a rotation period of 17.4 hr, TOI 540 is rotating more rapidly than TRAPPIST-1, the only other rapidly rotating planet host within 15 pc. We complement TESS photometry with ground-based follow-up photometry from MEarth, confirming the planetary nature of the candidate. In addition, we present RV measurements from CHIRON and the High Accuracy Radial velocity Planet Searcher (HARPS), speckle imaging from the Southern Astrophysical Research (SOAR) Telescope, and X-ray data from XMM-Newton and ROSAT.

2. Properties of the Host Star

TOI 540, otherwise known as 2MASS J05051443-4756154 (Skrutskie et al. 2006) and UCAC4 211-005570 (Finch et al. 2014), is a nearby main-sequence M dwarf. Based on the parallax measurement of $\pi = 71.3886 \pm 0.0448$ mas reported in Gaia DR2 (Gaia Collaboration et al. 2018; Lindgren et al. 2018), we calculate a distance of $d = 14.0078 \pm 0.0088$ pc

from Earth. TOI 540 has a low proper motion for a nearby star ($\mu_{\alpha} = -66.09 \pm 0.08$ mas yr⁻¹, $\mu_{\delta} = 25.08 \pm 0.09$ mas yr⁻¹) which likely prevented it from being widely identified as a nearby star before Gaia. The proper motion is also too low to rule out the presence of background stars from archival images (in Section 3.4 we present high-angular-resolution images that rule out the presence of other bright stars in the immediate vicinity). To obtain an estimate for the mass of the star, we use the mass–luminosity relationship for main-sequence M dwarfs in Benedict et al. (2016) and the K-band apparent magnitude of 8.900 ± 0.021 from the Two Micron All-Sky Survey (2MASS). This yields a stellar mass of $M = 0.159 \pm 0.014 M_{\odot}$. We determine the stellar radius using two different mass–radius relations: one determined from optical interferometry of single stars in Boyajian et al. (2012), and another from eclipsing binary measurements in Bayless & Orosz (2006). The former yields $R = 0.195 \pm 0.011 R_{\odot}$ and the latter produces $R = 0.182 \pm 0.013 R_{\odot}$. We then calculate a weighted average of the two estimates, obtaining $R = 0.190 \pm 0.008 R_{\odot}$. We note that this is also consistent with the radius–luminosity relation in Mann et al. (2015), which predicts $R = 0.197 \pm 0.007 R_{\odot}$. Informed by these relationships, we refine our estimate of the stellar radius using transit geometry in Section 4 and report the final value in Table 3.

In order to determine the color indices of TOI 540, we adopt the *J*-, *H*-, and *K_S*-band magnitudes from 2MASS (Skrutskie et al. 2006), and we obtained *V_JR_{KC}I_{KC}*-photometry from the REsearch Consortium On Nearby Stars (RECONS).¹⁵ The *VRI* photometry was collected on the night of 2019 August 20, with exposure times of 300, 180, and 75 s, respectively. The RECONS fluxes were extracted using a 4'' radius aperture to minimize contamination from a nearby background star, described in Section 2.1. The *VRI* magnitudes for TOI 540 are reported in Table 3.

The luminosity of TOI 540 can be estimated from bolometric corrections (BC). In particular, interpolating between the *BC_V* values as a function of *V* – *K_S* in Table 5 of Pecaut & Mamajek (2013) yields a bolometric correction of *BC_V* = –2.938, corresponding to a luminosity of $L = 0.003745 L_{\odot}$. Alternatively, using the derived third-order polynomial fit between *BC_J* and *V* – *J* in Mann et al. (2015, and its erratum), we obtain *BC_J* = 1.951, which gives us a luminosity of $L = 0.003254 L_{\odot}$. Finally, we use the relationship between *BC_K* and *I* – *K* in Leggett et al. (2001) to produce *BC_K* = 2.764 and $L = 0.003383 L_{\odot}$. We take as our final value the mean and the standard deviation of the three luminosity estimates, $L = 0.00346 \pm 0.00021 L_{\odot}$. This allows us to use the Stefan-Boltzmann law to determine the effective stellar temperature via $T_{\text{eff}} = T_{\text{eff},\odot}(L/L_{\odot})^{1/4}(R/R_{\odot})^{-1/2}$, yielding $T_{\text{eff}} = 3216 \pm 83$ K. We adopted the solar values of $M_{\text{bol},\odot} = 4.7554$ mag and $T_{\text{eff},\odot} = 5772$ K cited in Mamajek (2012).

Due to the slow evolution of M dwarfs in their rapid rotation stage, we are unable to place tight constraints on the age of the system. However, we note that TOI 540 is not overluminous (based on the observed color and luminosity), and therefore it is likely to be on the main sequence, implying an age greater than 100 Myr (Baraffe et al. 2002). Based on the galactic space velocity *W* and established age–velocity relations, and the observed rapid stellar rotation, we can place an upper limit of

¹⁵ www.recons.org

2 Gyr on the system (Newton et al. 2016). We also estimate the average equivalent width of $H\alpha$ emission from the four CHIRON spectra described in Section 3.3 to be $2.8 \pm 0.1 \text{ \AA}$, consistent with TOI 540 not being a pre-main-sequence star. Finally, we use BANYAN Σ (Gagné et al. 2018) to investigate TOI 540's potential membership of young stellar associations based on its location in XYZUVW space (calculated from the coordinates, proper motion, and RV values), and rule out 27 well-characterized young associations within 150 pc with 99.9% confidence.

TOI 540 is a highly magnetically active star as indicated by the photometric modulation due to stellar spots and the numerous flares present in each sector of the TESS data. Measuring how often TOI 540 flares is essential to understanding the environment in which its planet resides. The flare frequency distribution describes the rate of flares as a function of energy and follows the probability distribution $N(E)dE = \Omega E^{-\alpha} dE$ (Lacy et al. 1976, Equation (2)) where α is the slope of the power law and Ω is a normalization constant. Using the methods outlined in Medina et al. (2020), we find $\alpha = 1.97$ and measure a rate of 0.12 flares per day above an energy of $E = 3.16 \times 10^{31}$ erg in the TESS bandpass. Medina et al. (2020) find that TOI 540 has a flare rate that is consistent with other stars of a similar mass and rotation period.

2.1. A Neighboring Star 6'' Away

Our efforts are complicated by a neighboring background star at a distance of 6'' from TOI 540. We first noticed this background source in MEarth follow-up photometry (described in Section 3.2) and subsequently identified it in Gaia DR2. It has a Gaia ID of 4785886975670558336 and is 2.26 mag fainter than the main target in the G_{BP} passband. While both the neighboring star and TOI 540 occupy the same TESS pixel, we are able to resolve the two stars using MEarth photometry and confirm that the planet does indeed transit TOI 540. In particular, we extract the light curve of TOI 540 using variable aperture sizes and find that the transit persists with a similar depth down to an aperture of 2''.5, a size small enough to exclude the neighboring star.

3. Observations

3.1. TESS Photometry

TESS collected photometry of TOI 540 in observation sectors 4, 5, and 6, with the observations spanning a nearly three-month period from 2018 October 19 to 2019 January 6. The star was included in the TESS Input Catalog (TIC) with a TIC ID of 200322593 as well as the TESS Candidate Target List (CTL; Stassun et al. 2018), and TESS Guest Investigator programs G011180 (PI: Courtney Dressing) and G011231 (PI: Jennifer Winters). We utilize the two-minute cadence presearch data conditioning (PDCSAP; Smith et al. 2012; Stumpe et al. 2012, 2014) light curve reduced with the NASA Ames Science Processing Operations Center (SPOC) pipeline (Jenkins et al. 2016). The PDCSAP fluxes have been corrected for instrumental systematic effects as well as crowding: unresolved light from other nearby stars listed in the TIC v7. While the background source from Section 2.1 is listed in version 8 of the TIC, it did not appear in version 7 that was used to reduce the TESS photometry presented in this work. Based on TIC v8, the background star is 4.46 mag fainter than TOI 540 in the TESS

bandpass. This leads to an error of 1.6% in the measured transit depth, or 0.8% in the planetary radius. The latter is much smaller than the final uncertainty of 5.8% derived in this work (Table 5). Therefore, we have not corrected the TESS light curve presented in Section 3.1 for the additional flux dilution due to this neighboring source.

A planetary candidate with an orbital period of 1.239 days was initially detected by the SPOC in sector 4 data validation reports (DVR; Twicken et al. 2018; Li et al. 2019) with a signal-to-noise ratio of 8.9, based on 16 transits. TESS ultimately observed 50 transits of TOI 540 b over the three sectors, with an average transit depth of 2168 ± 172 ppm, yielding a signal-to-noise ratio of 15.6. However, the correct spectral type and stellar radius was undefined in the TIC (v7) and therefore assumed to be $1 R_{\odot}$ during the preparation of the DVR, leading to a substantially overestimated planetary radius of $5 R_{\oplus}$.

We make use of the full PDCSAP light curve from which we remove bright outliers (more than 0.02 mag brighter than the mean flux) that constitute 0.099% of the total TESS data and may be caused by contamination from flares. The data clipping is done to ensure consistency between the handling of TESS and MEarth data sets (see Section 3.2). The final TESS light curve consists of 48,445 individual data points, and can be seen in Figure 1. We note that per the TESS data release notes of sector 4,¹⁶ an interruption in communications between the instrument and spacecraft resulted in an instrument turn-off for 2.7 days, during which no data were collected.

3.2. MEarth Follow-up Photometry

Using the eight 40 cm aperture telescopes of the MEarth-South telescope array at the Cerro Tololo International Observatory (CTIO) in Chile (Nutzman & Charbonneau 2008; Irwin et al. 2015), we conducted follow-up observations of TOI 540 to confirm the transits of the terrestrial planet. The MEarth-South telescopes employ a custom bandpass centered at the red end of the optical spectrum (similar to TESS). We observed 10 transits of TOI 540 b between 2019 July 27 and 2019 December 8, using an exposure time of 40 s per measurement. However, we discarded the data from the transit on December 8 due to a stellar flare shortly following the transit egress, which would have led to needless challenges in modeling the out-of-transit flux baseline. Therefore, we proceeded by including the data from the first nine transits only. Aperture photometry was carried out in all images using a fixed aperture radius of 6 pixels, or 5''.1. After excluding outliers 0.02 mag brighter than the mean flux (0.068% of the data set), the MEarth light curve contains a combined 17,879 data points from all eight telescopes. The individual light curves from each visit are shown in Figure 2.

3.3. CHIRON and HARPS Spectroscopy

We gathered four reconnaissance spectra of TOI 540 with the CHIRON spectrograph (Tokovinin et al. 2013) mounted on the CTIO/Small and Moderate Aperture Research Telescope System (SMARTS) 1.5 m telescope at CTIO. The spectra were accumulated as part of a nearly volume-complete spectroscopic survey of nearby mid-to-late M dwarfs. The methods by which we determined the RVs and rotation broadening, below, are described in Winters et al. (2020). The observations were

¹⁶ https://archive.stsci.edu/missions/tess/doc/tess_dm/tess_sector_04_dm05_v04.pdf

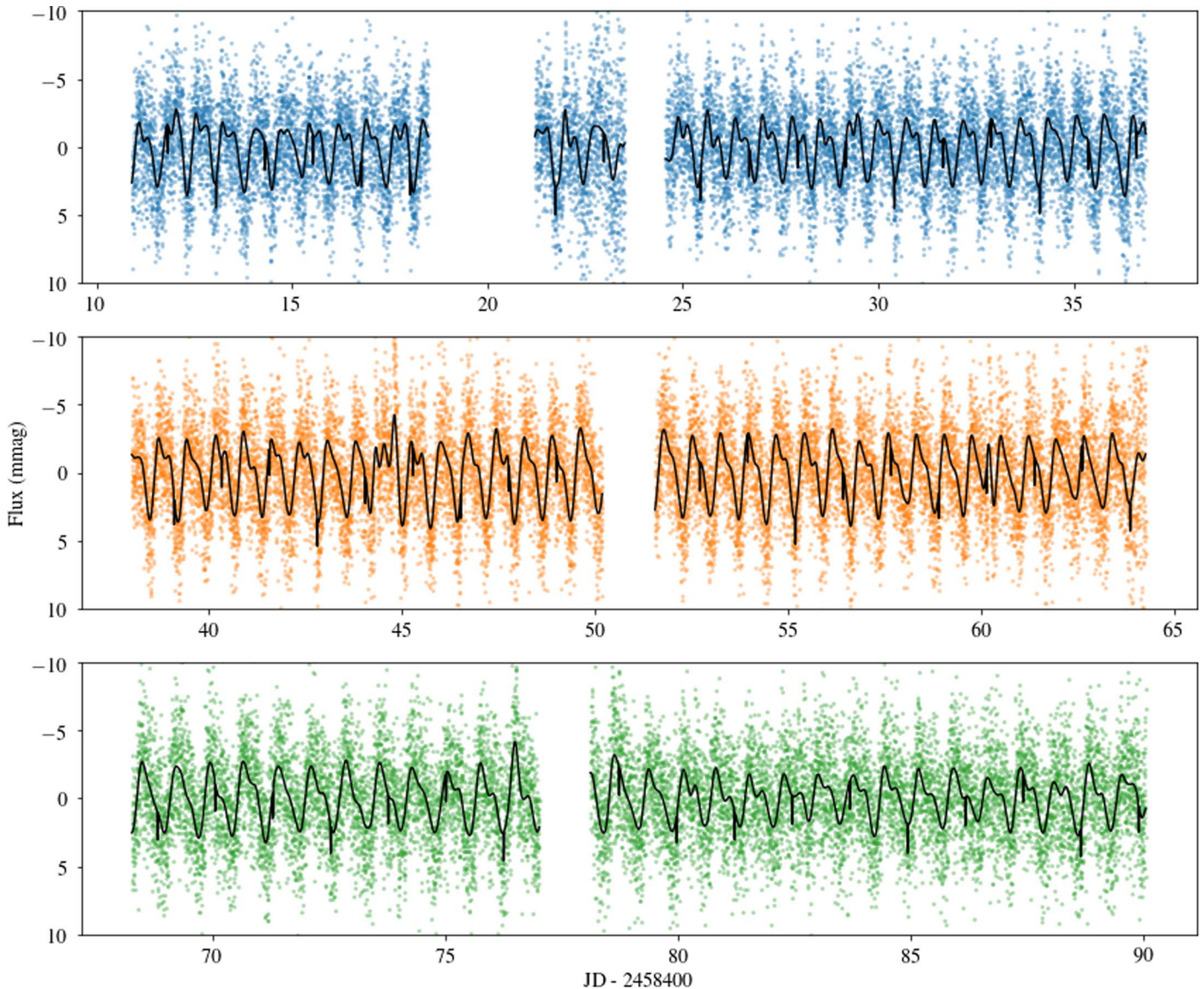


Figure 1. TESS photometry of TOI 540 from sectors 4 (blue), 5 (orange), and 6 (green). The combined transit and stellar rotation model from Section 4 is overlotted as a solid line.

(The data used to create this figure are available.)

carried out between 2018 September and 2019 November in 3×20 minutes exposures per observation, employing the image slicer mode for a resolution of $R = 80,000$. We obtained multi-order RVs from six spectral orders (see Table 1) as well as an estimated projected rotation velocity of $v \sin i = 13.98 \text{ km s}^{-1}$. In addition, we collected three spectra using the HARPS spectrograph (Mayor et al. 2003) mounted on the ESO 3.6 m telescope at La Silla. The HARPS spectrograph has a measured spectral resolution of $R = 120,000$. The observations were carried out in 2019 April (ESO HARPS Program 0103.C-0442, PI: Díaz) with a 30 minute exposure time. We estimated the RVs by combining 21 spectral orders and calculated a $v \sin i$ of 12.93 km s^{-1} . The RVs are displayed in Figure 3.

We adopt the mean of the two rotation velocity estimates as our final value, obtaining $v \sin i = 13.5 \pm 1.5 \text{ km s}^{-1}$. This yields a rotation period estimate of $\frac{P_{\text{rot}}}{\sin i} = \frac{2\pi R}{v \sin i} = 0.71 \pm 0.08$ days, consistent with the photometrically determined rotation period of 0.72610 day from Section 4 for $\sin i \approx 1$, suggesting

that the inclination of the rotation axis is close to 90° , and that the stellar obliquity is low. The $v \sin i$ values for both CHIRON and HARPS were generated by applying appropriate rotational broadening to an observed M-dwarf spectrum.

We note that our RV measurements have uncertainties greater than 100 m s^{-1} , estimated from theoretical uncertainties for a rotating star (e.g., Bouchy et al. 2001) with inflation to account for RV scatter in between the spectral orders. The large uncertainties are driven by the low signal-to-noise ratios of the spectra (typically 5–10) due to the star being substantially redder than what is optimal for the spectrographs and settings that were used to collect these spectra. The HARPS spectra were gathered in the simultaneous reference mode using a Thorium–Argon lamp which significantly degrades the spectrum in the red orders. Rotational broadening of spectral lines also contributes to the degradation of RV precision. The reported errors are on par with the rms of the RVs (163 m s^{-1}).

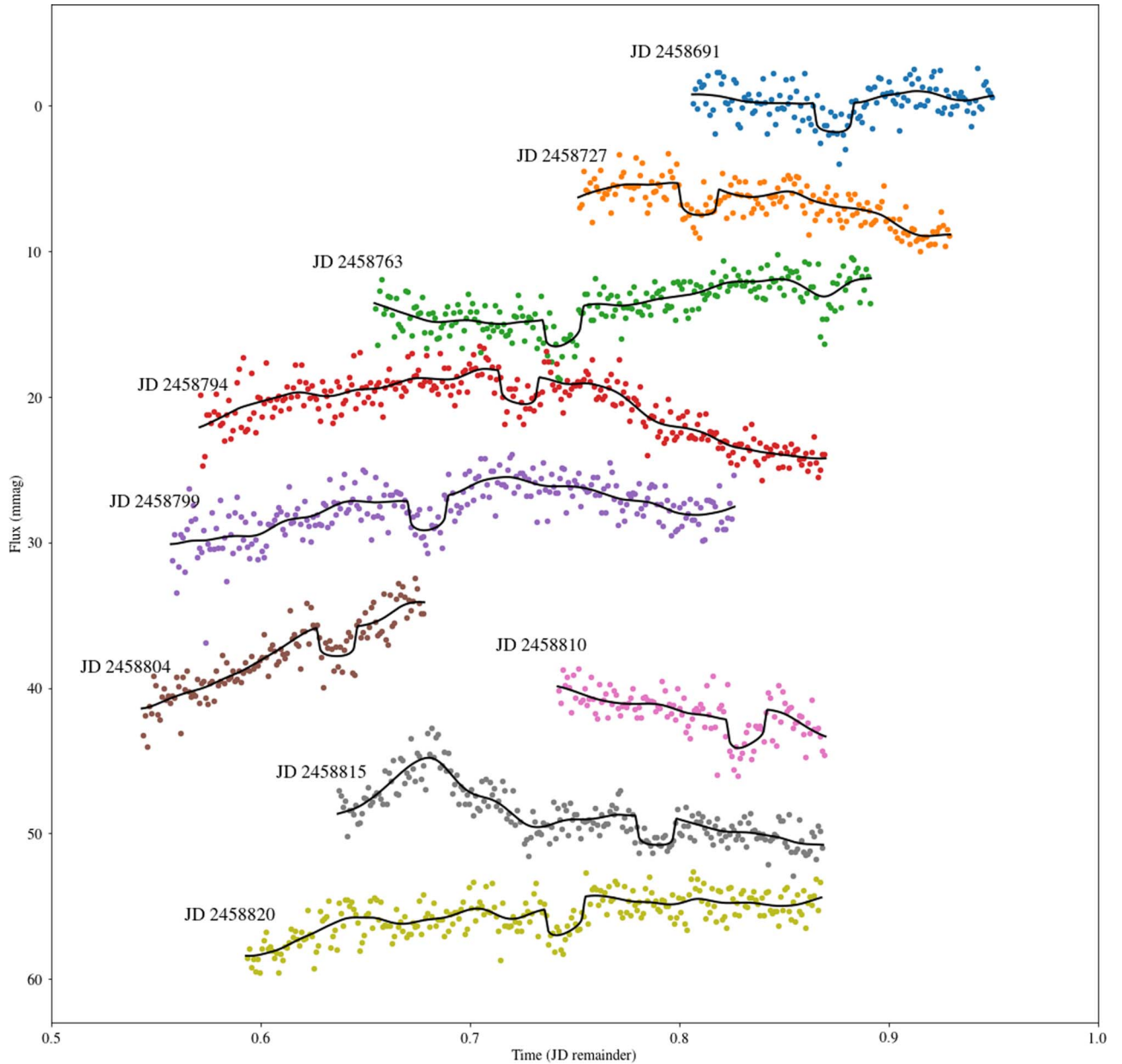


Figure 2. Follow-up photometry of TOI 540 from all eight MEarth telescopes by night. The data has been combined and binned to a cadence of 1.44 minutes. The solid line represents the combined transit and baseline model from Section 4.

(The data used to create this figure are available.)

Table 1
RV Data for TOI 540

BJD (TDB)	RV (km s^{-1})	Uncertainty (km s^{-1})	Instrument
2458385.8447	18.5791	0.142	CHIRON
2458576.5615	18.9040	0.1886	HARPS
2458578.5499	18.4817	0.1375	HARPS
2458579.5788	18.6201	0.1221	HARPS
2458607.4689	18.7156	0.133	CHIRON
2458801.6815	18.3476	0.195	CHIRON
2458803.5955	18.5508	0.194	CHIRON

(This table is available in machine-readable form.)

Employing the estimated mass of the planet from Section 5, the RV semi-amplitude for TOI 540 b corresponding to a circular orbit would be $K = 1.4 \pm 0.3 \text{ m s}^{-1}$. Therefore, the rapid rotation of the star makes direct mass measurements with RVs currently unfeasible. However, the RVs help rule out a close-in massive companion: the standard deviation of all seven measurements is 167 m s^{-1} , close to the individual uncertainties, and there is no evidence of a trend. In particular, we are able to rule out a companion with a mass of $m > 0.73M_{\text{Jup}}$ at the orbital period of the transiting planet with 99.7% (3σ) confidence. This was estimated by fitting an RV model with the period, epoch, and eccentricity fixed to the values in Table 3, and calculating the appropriate semi-amplitude for which the cumulative distribution function (CDF) of the χ^2 distribution has a p -value below 0.0027.

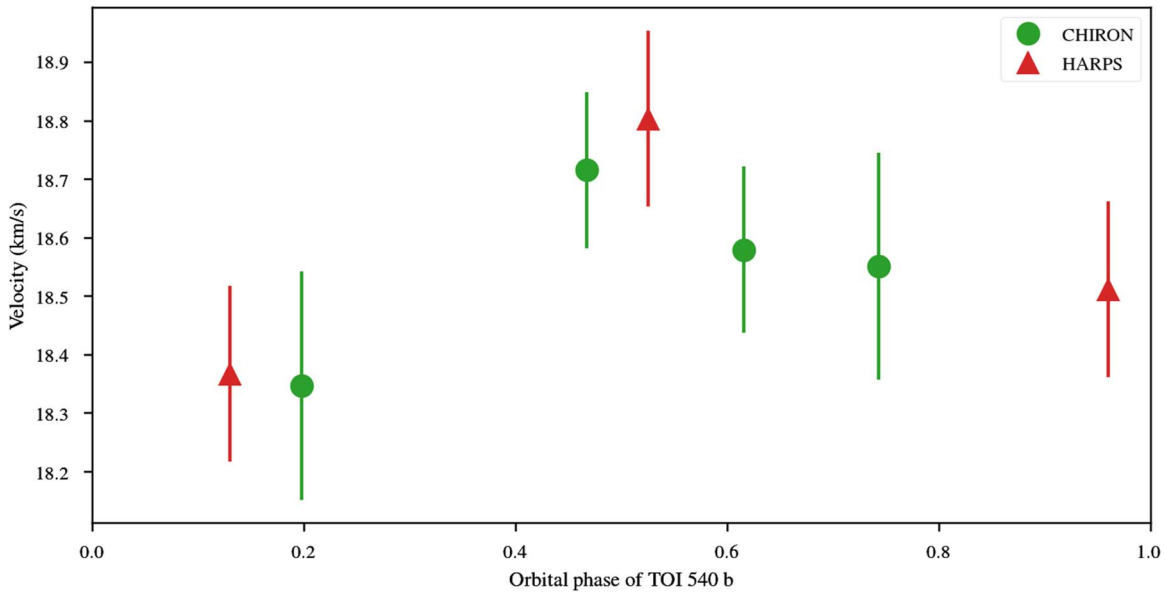


Figure 3. RV measurements of TOI 540 from CHIRON and HARPS as a function of orbital phase, with phase of zero corresponding to the time of transit. There is no evidence for a significant trend caused by a massive companion. The expected RV semi-amplitude for TOI 540 b is $K = 1.4 \pm 0.3 \text{ m s}^{-1}$ (assuming a circular orbit), well below the precision of the currently available data.

3.4. SOAR Speckle Imaging

Nearby stars that fall within the same $21''$ TESS pixel as the target can cause photometric contamination or be the source of an astrophysical false positive. We searched for nearby sources to TOI 540 with SOAR speckle imaging (Tokovinin 2018) on 2019 July 14 UT, observing in the visible I bandpass. Details of the observation are available in Ziegler et al. (2020). We detected no nearby sources within $3''$ of TOI 540, corresponding to a projected distance of 42 au. The 5σ detection sensitivity and the speckle autocorrelation function (contrast curve) from the SOAR observation are plotted in Figure 4.

3.5. X-Ray Detections by XMM-Newton and ROSAT

A testament to its significant X-ray brightness, TOI 540 was detected by XMM-Newton during a slew operation on 2004 July 27. The detection appears in the XMM slew 2 catalog with a source ID of XMMSL2 J050514.2-475618 (slew obs. ID 9084800002). The flux of the target is listed as $(1.43 \pm 0.50) \times 10^{-12} \text{ erg s}^{-1} \text{ cm}^{-2}$ in the soft 0.2–2 keV bandpass and $(3.91 \pm 1.35) \times 10^{-12} \text{ erg s}^{-1} \text{ cm}^{-2}$ in the total 0.2–12 keV bandpass. No detection is listed separately in the hard 2–12 keV bandpass. For consistency with Wright et al. (2018), we convert the soft bandpass flux into the ROSAT bandpass of 0.1–2.4 keV. We use the astrophysical plasma emission code (APEC)¹⁷ model at solar abundance and a plasma temperature of $kT = 0.54 \text{ keV}$. The conversion is done using the portable interactive multi-mission simulator (PIMMS)¹⁸ and yields an X-ray flux of $(1.60 \pm 0.56) \times 10^{-12} \text{ erg s}^{-1} \text{ cm}^{-2}$ in the ROSAT bandpass. This corresponds to an X-ray-to-bolometric luminosity ratio of $L_X/L_{\text{bol}} = 0.0028$, consistent with $L_X/L_{\text{bol}} \simeq 10^{-3}$ measured by Wright et al. (2018) for rapidly rotating stars. The implications of this are further discussed in Section 5.

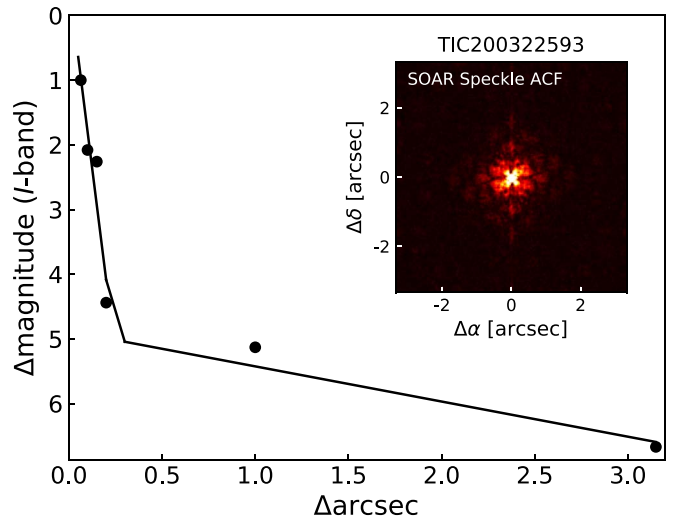


Figure 4. The 5σ detection sensitivity (solid line) and the autocorrelation function (ACF, inset) of TOI 540 from SOAR speckle imaging showing no evidence of nearby light sources.

TOI 540 also appears in the second ROSAT all-sky survey source catalog (Boller et al. 2016) with a source name of J050514.2-475625. It was observed by ROSAT in 1990 August with a count rate of $0.0413 \pm 0.0176 \text{ counts s}^{-1}$ in the 0.1–2.4 keV energy band. Using the aforementioned APEC model leads to a somewhat lower X-ray flux estimate of $3 \times 10^{-13} \text{ erg s}^{-1} \text{ cm}^{-2}$; however, the error on the count rate is substantial.

4. Modeling of TESS and MEarth Light Curves

We analyze the MEarth and TESS light curve data simultaneously with the Python package *exoplanet* (Foreman-Mackey et al. 2019), which is a framework built on the Hamiltonian Monte Carlo methods implemented in PyMC3 (Salvatier et al. 2016) via Theano (Theano Development Team 2016) for computationally efficient sampling.

¹⁷ <http://www.atomdb.org/>

¹⁸ <https://heasarc.gsfc.nasa.gov/docs/software/tools/pimms.html>

Table 2
Model Parameters for Light Curve Fitting

Parameter	Explanation	Prior	Value	Units
μ_{TESS}	TESS flux baseline	$\mathcal{N}(0, 10)$	-0.025 ± 0.025	mmag
$\ln \sigma_{\text{TESS}}^2$	TESS excess white noise	$\mathcal{N}(\ln 6.76, 5)$	-8.44 ± 2.04	mmag ²
μ_{MEarth}	MEarth flux baseline	$\mathcal{N}(0, 10)$	-0.49 ± 0.40	mmag
$\ln \sigma_{\text{MEarth}}^2$	MEarth excess white noise	$\mathcal{N}(\ln 3.44, 5)$	1.154 ± 0.028	mmag ²
M	Stellar mass	$\mathcal{N}(0.159, 0.014)$	Table 3	M_{\odot}
R	Stellar radius	$\mathcal{N}(0.190, 0.008)$	Table 3	R_{\odot}
$\ln Q_0$	Quality parameter	$\mathcal{N}(1, 10)$	1.07 ± 0.19	...
$\ln \Delta Q$	Quality parameter	$\mathcal{N}(2, 10)$	7.88 ± 0.80	...
$\ln P_{\text{rot}}$	Stellar rotation period	$\mathcal{N}(\ln 0.7266, 0.01)$	Table 3	days
$\ln \mathcal{A}$	Covariance amplitude	$\mathcal{N}(\ln 10.62, 5)$	0.54 ± 0.63	mmag ²
λ	Covariance amp. ratio	$\mathcal{U}(0, 1)$	0.54 ± 0.25	...
$\ln \sigma^2$	Covariance amplitude	$\mathcal{N}(\ln 16.84, 5)$	0.711 ± 0.080	mmag ²
ρ	Covariance decay timescale	$\mathcal{N}(0.036, 0.0036)$	0.0463 ± 0.0028	days
t_0	Transit midpoint	$\mathcal{N}(2458411.8264, 0.1)$	Table 3	BJD
$\ln P$	Orbital period	$\mathcal{N}(\ln 1.23913, 0.01)$	Table 3	days
r/R	Planet-star radius ratio	$\mathcal{U}(0.01, 0.4)$	Table 3	...
b	Impact parameter	$\mathcal{U}(0, 1 + r/R)$	Table 3	...

Note. $\mathcal{N}(\mu, \sigma)$ denotes a normal distribution. $\mathcal{U}(a, b)$ denotes a uniform distribution.

Importantly, `exoplanet` extends the basic support for Gaussian process (GP) modeling in `PyMC3` by implementing scalable GPs through `celerite` (Foreman-Mackey 2018), which makes the otherwise notoriously slow GP modeling much more tractable. Our model has multiple components that are optimized simultaneously, described in the following sections.

We model the rotational modulation in the TESS photometry with a GP employing `exoplanet`'s Rotation kernel, which has a covariance function that is a sum of two stochastically driven harmonic oscillators (SHO),

$$k_{\text{TESS}}(\tau; Q_0, \Delta Q, P_{\text{rot}}, \mathcal{A}, \lambda) = k_{\text{SHO}}(\tau; Q_1, \omega_1, S_1) + k_{\text{SHO}}(\tau; Q_2, \omega_2, S_2) \quad (1)$$

$$Q_1 = \frac{1}{2} + Q_0 + \Delta Q \quad Q_2 = \frac{1}{2} + Q_0$$

$$\omega_1 = \frac{4\pi Q_1}{P_{\text{rot}} \sqrt{4Q_1^2 - 1}} \quad \omega_2 = \frac{8\pi Q_2}{P_{\text{rot}} \sqrt{4Q_2^2 - 1}}$$

$$S_1 = \frac{\mathcal{A}}{\omega_1 Q_1} \quad S_2 = \frac{\lambda \mathcal{A}}{\omega_2 Q_2},$$

where the covariance function of a single SHO is given by

$$k_{\text{SHO}}(\tau; Q, \omega, S) = S\omega Q e^{-\frac{\omega\tau}{2Q}}$$

$$\times \begin{cases} \cosh(\eta\omega\tau) + \frac{1}{2\eta Q} \sinh(\eta\omega\tau) & \text{if } 0 < Q < 1/2 \\ 2(1 + \omega\tau) & \text{if } Q = 1/2 \\ \cos(\eta\omega\tau) + \frac{1}{2\eta Q} \sin(\eta\omega\tau) & \text{if } Q > 1/2 \end{cases} \quad (2)$$

with $\eta \equiv \sqrt{\left|1 - \frac{1}{4Q^2}\right|}$. Thus, the rotation kernel has five parameters: the quality factors Q_0 and ΔQ , the rotation period P_{rot} , the primary amplitude \mathcal{A} , and the amplitude ratio λ . We note that the two SHO components correspond to the first and second harmonics of the oscillation, with the latter having twice the frequency (or equivalently, half the period) of the former. This type of kernel has been shown to successfully

model a range of complicated rotationally modulated signals (Haywood et al. 2014; Soto et al. 2018; Winters et al. 2019; Cloutier et al. 2020b). The parameters of the kernel are constrained with normal and uniform prior distributions, documented in Table 2. We obtain an initial estimate of 17.4 hr for P_{rot} by fitting a sum of two sinusoids to the TESS light curve, and we subsequently constrain P_{rot} with a normal prior distribution centered at that value. The prior for \mathcal{A} is centered at the value corresponding to the variance of the observed TESS light curve. We note that since Q_0 will always be positive with this setup, the quality parameters Q_1 and Q_2 of both SHOs are guaranteed to remain above one-half in Equation (2).

The MEarth follow-up photometry is modeled with a separate covariance kernel. This is due to the additional contribution from precipitable water vapor that induces strong nonlinear trends into the individual light curves of each night. The form of the kernel is

$$k_{\text{MEarth}}(\tau; \sigma, \rho) = \frac{\sigma^2}{2} \left[\left(1 + \frac{1}{\epsilon}\right) e^{-(1-\epsilon)\sqrt{3}\tau/\rho} + \left(1 - \frac{1}{\epsilon}\right) e^{-(1+\epsilon)\sqrt{3}\tau/\rho} \right] \quad (3)$$

which, for small values of ϵ , approximates the well-known Matérn-3/2 kernel

$$\lim_{\epsilon \rightarrow 0} k_{\text{MEarth}}(\tau; \sigma, \rho) = \sigma^2 \left(1 + \frac{\sqrt{3}\tau}{\rho}\right) e^{-\sqrt{3}\tau/\rho}. \quad (4)$$

Here, ϵ is fixed to a standard value of 0.01. The exact form of the Matérn-3/2 kernel (Equation (4)) cannot be implemented within the framework of `celerite`, and we therefore need to use the approximate form of Equation (3). The timescale parameter $\rho/\sqrt{3}$ is constrained with a Gaussian prior centered at 30 minutes, which we expect to be the typical minimum timescale for variations in precipitable water vapor in the atmosphere. The prior for σ is centered at the value corresponding to the

Table 3
System Parameters for TOI 540

Parameter	Values for TOI 540	Source ^a
Stellar parameters		
Right ascension (J2000)	05h 05 min 14.4 s	(1)
Declination (J2000)	-47° 56′ 15″.5	(1)
Proper motion (mas yr ⁻¹)	$\mu_{\alpha} = -66.09 \pm 0.08$ $\mu_{\delta} = 25.08 \pm 0.09$	(1)
Apparent brightness (mag)	$V_J = 14.492 \pm 0.03$	(3)
	$R_{KC} = 13.115 \pm 0.03$	(3)
	$I_{KC} = 11.402 \pm 0.03$	(3)
	$J = 9.755 \pm 0.022$	(2)
	$H = 9.170 \pm 0.022$	(2)
	$K_S = 8.900 \pm 0.021$	(2)
Distance (pc)	14.0078 ± 0.0088	(1)
Mass (M_{\odot})	0.159 ± 0.014	(3)
Radius (R_{\odot})	0.1895 ± 0.0079	(3)
Luminosity (L_{\odot})	0.00346 ± 0.00021	(3)
Fractional X-ray luminos- ity L_X/L_{bol}	0.0028	(3)
X-ray flux ^b (erg s ⁻¹ cm ⁻²)	$(1.60 \pm 0.56) \times 10^{-12}$	(3)
Effective temperature (K)	3216 ± 83	(3)
Age (Gyr)	0.1–2 Gyr	(3)
Rotational period (days)	0.72610 ± 0.00039	(3)
Projected rotation velocity (km s ⁻¹)	13.5 ± 1.5	(3)
Parameter	Values for TOI 540 b	
Modeled transit parameters		
Orbital period P (days)	1.2391491 ± 0.0000017	
Eccentricity e	0 (fixed)	
Time of mid-transit t_T (BJD)	2458411.82601 ± 0.00046	
Impact parameter b	0.772 ± 0.029	
Planet-to-star radius ratio r/R	0.0436 ± 0.0012	
a/R ratio	13.90 ± 0.72	
Derived planetary parameters		
Radius r (R_{\oplus})	0.903 ± 0.052	
Semimajor axis a (au)	0.01223 ± 0.00036	
Inclination i (deg)	86.80 ± 0.28	
Bolometric incident flux S (S_{\oplus})	23.4 ± 2.1	
Equilibrium temperature ^c T_{eq} (K)	611 ± 23	

Notes.

^a (1) Gaia Collaboration et al. (2018), (2) Skrutskie et al. (2006), (3) this work.

^b The X-ray flux is given in the ROSAT bandpass of 0.1–2.4 keV.

^c The equilibrium temperature assumes a Bond albedo of zero. For an albedo of A_B , the reported temperature has to be multiplied by $(1 - A_B)^{1/4}$.

variance of the observed MEarth light curve. We note that due to the estimated stellar rotation period of 17.4 hr, the kernel in Equation (3) is also able to absorb the rotational modulation with the exponential decay timescale being much shorter than the rotation period, whereas a quasi-periodic kernel (such as Equation (1)) would be misled by the nonperiodic changes in the water vapor content. We did experiment with a kernel that combined both a quasi-periodic and a Matérn-3/2 term, but we ultimately found it impossible to decouple the effects of stellar rotation and water vapor variations in a statistically significant way. Thus, the Matérn-3/2 kernel is our preferred model to account for both periodic as well as nonperiodic modulations in the high-cadence but short-baseline MEarth follow-up data.

Transits of TOI 540 b are modeled using the `starry` module (Luger et al. 2019) included in `exoplanet`. A single transit

model is fitted simultaneously to TESS and MEarth photometry. While the model presented here does not account for the non-zero exposure times, we did test a model light curve that was oversampled and integrated over the different exposures (also with `exoplanet`) and found the differences to be negligible. The free parameters in the model are the transit midpoint t_0 , the orbital period P , the planet-to-star radius ratio r/R , and the impact parameter b . The first two (t_0 and P) are constrained relatively tightly with Gaussian priors since they can be pre-determined with good precision from the TESS data alone. The two-dimensionless parameters (r/R and b) have uniform prior distributions. We also include quadratic limb-darkening, with the appropriate coefficients adopted from Table 5 of Claret (2018) for the spherical PHOENIX-COND limb-darkening model (Husser et al. 2013). In particular, we use $a = 0.1553$ and $b = 0.4742$, corresponding to a local gravity of $\log g = 5.0$, an effective temperature of 3200 K, and the TESS bandpass. We separately estimated the limb-darkening coefficients for the MEarth optical filter following the process outlined in Section 6.1 of Irwin et al. (2018). However, due to the similarity between the MEarth and TESS bandpasses, we found no meaningful difference between using either set of limb-darkening coefficients: the resulting discrepancy in the modeled light curve was orders of magnitude smaller than the measurement uncertainty. Therefore, we decided to simplify the modeling by adopting the TESS limb-darkening coefficients given above for both data sets.

In addition, we allow for a baseline flux as well as additional white noise (added in quadrature to each individual flux uncertainty) in the TESS and MEarth data as additional model parameters. They are loosely constrained with Gaussian prior distributions. The priors for excess white noise are centered at the values corresponding to the smallest individual flux uncertainties in the respective data sets. A comprehensive list of all model parameters is given in Table 2.

We note that our reported model assumes a circular orbit (zero eccentricity). Due to the short orbital period of the planet, it is reasonable to expect that tidal dissipation has damped any initial amount of orbital eccentricity to an undetectably small level. Based on the work of Goldreich & Soter (1966), the expected tidal circularization timescale is close to 150,000 yr (assuming the estimated bulk density from Section 5 and a specific dissipation function of $Q = 100$, which is appropriate for terrestrial planets), much shorter than the expected age of the system. Allowing the eccentricity e and the angle of periastron passage ω to fluctuate produces a posterior probability distribution that is consistent with $e = 0$ at the cost of significantly broadening the posterior distributions of several other parameters (such as the impact parameter b) that alter the light curve in a similar way. Since an eccentricity much greater than zero would be inconsistent with the tidal circularization timescale, we keep e fixed to zero to constrain the other parameters better.

We proceed to tune and sample the model posterior distributions with `PyMC3`. The Markov Chain Monte Carlo (MCMC) sampling is done in parallel in four independent chains. Sampling from each chain begins with a burn-in phase of 1000 steps with an automatically tuned step size such that the acceptance fraction approaches 90%, which facilitates convergence in complicated posterior distributions. We draw 1000 samples from each chain, for a total of 4000 samples. The sample distributions from each chain can be compared to each

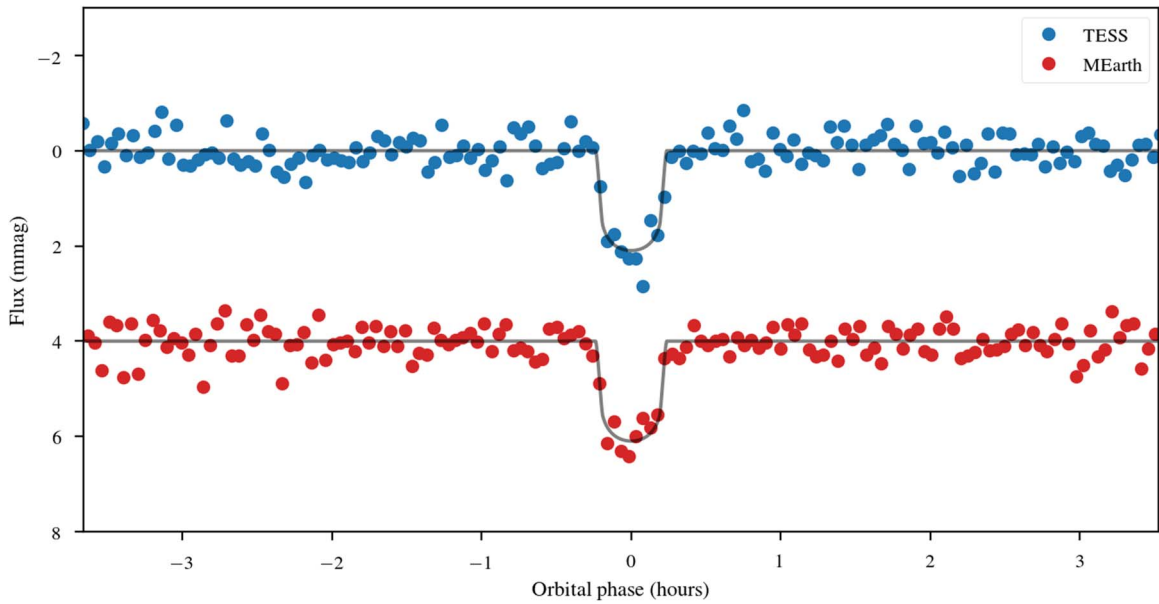


Figure 5. A phase-folded transit model of TOI 540 b from Section 4 overlaid on detrended TESS and MEarth data. Both data sets have been binned to 2.88 minute intervals for visual clarity. The number of transits fitted is 50 for the TESS data and 9 for MEarth.

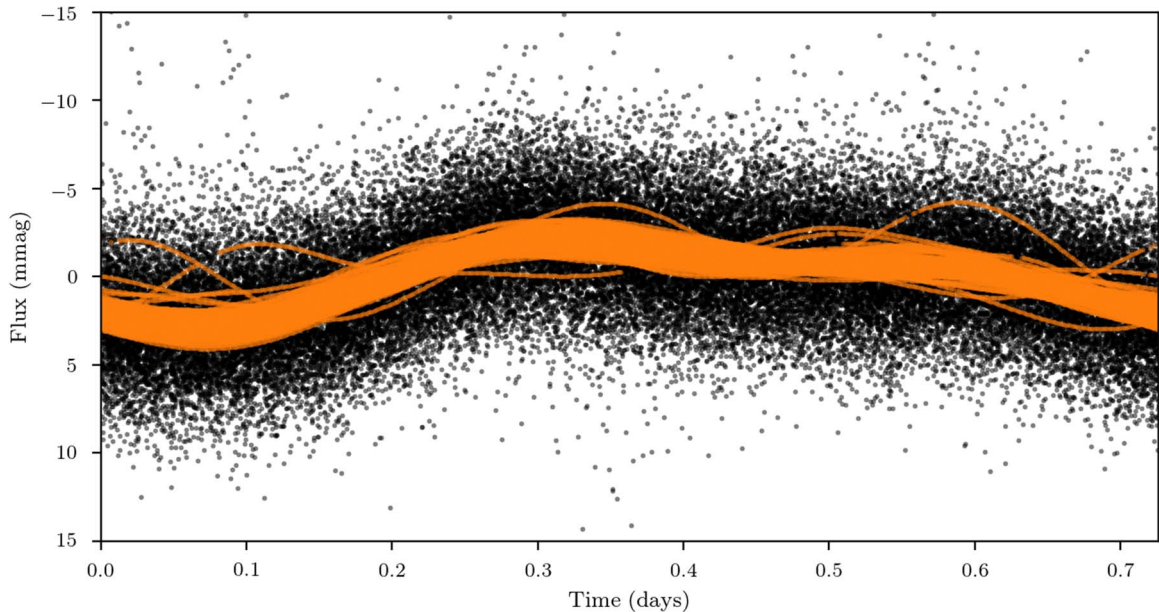


Figure 6. TESS photometry of TOI 540, phase-folded to the rotation period in Table 3. Solid orange lines overlay the data points, depicting the predicted rotational modulation for each individual observed stellar rotation. The orange curves overlap for the most part, implying that there is no evidence for long-term evolution in the modulation pattern, e.g., due to changes in the starspot coverage.

other to detect possible issues related to convergence. We detect no such problems: the resulting parameter distributions from the four chains are all consistent with one another. We report the means and the standard deviations of the modeled transit parameters from the 4000 samples in Table 3 as well as the rest of the parameters (including hyperparameters) in Table 2. The results of the modeling are described in detail in Section 5, and the modeled light curve can be seen overlaid on top of the TESS and MEarth raw data in Figures 1 and 2, respectively.

5. Discussion and Conclusion

TOI 540 b completes a trip around its rapidly rotating host star once every $P = 1.239149$ days (± 170 ms). The transits are not grazing with an impact parameter of $b = 0.772 \pm 0.029$, corresponding to an inclination angle of $i = 86^{\circ}80 \pm 0^{\circ}28$. The planet has a radius of $r = 0.903 \pm 0.052 R_{\oplus}$, slightly less than that of Venus. Based on its small radius, the planet is likely to be terrestrial for the reasons outlined in Section 1. Using Earth’s core mass fraction and a semi-empirical mass–radius relation for rocky planets by Zeng et al. (2016) yields an estimated mass of $m = 0.69 \pm 0.15 M_{\oplus}$ and a bulk density of $\rho = 5.2 \pm 1.4 \text{ g cm}^{-3}$. This corresponds to a surface gravity of $g = 8.3 \pm 2.0 \text{ m s}^{-2}$. Figure 5 displays the predicted transits

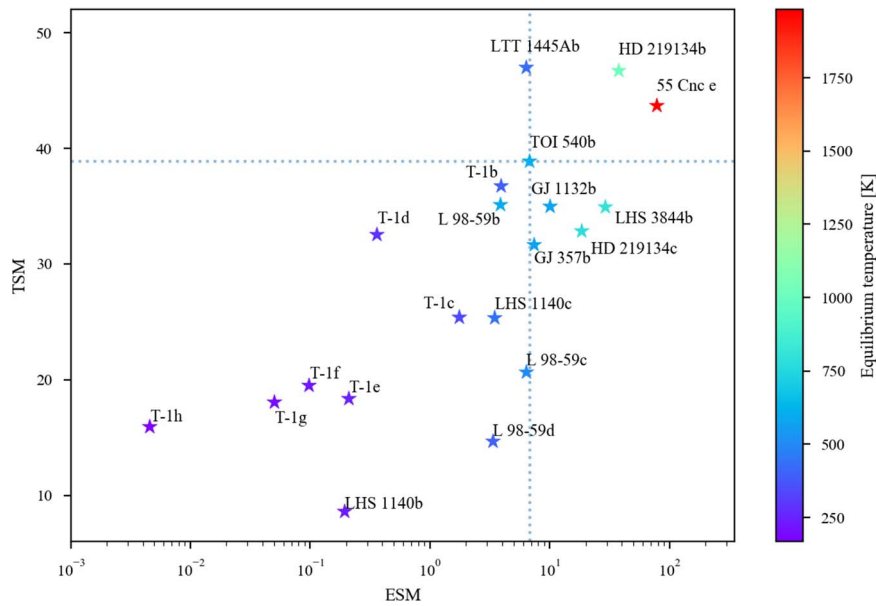


Figure 7. Estimated ESM and TSM values (Kempton et al. 2018) for the known terrestrial transiting planets within 15 pc of the Sun, highlighting the most promising nearby targets for emission and transmission spectroscopy. Crucially, the two best targets in the top right (55 Cnc e and HD 219134 b) orbit larger K dwarfs and may not be detectable by JWST once a systematic noise floor is taken into account. The color bar represents the equilibrium temperature of the planets assuming zero albedo and full day–night heat redistribution according to Equation (3) of Kempton et al. (2018). The TSM values were calculated with a scale factor of 0.190, calibrated for small planets. The dotted lines accentuate the location of TOI 540 b. The values for all parameters were adopted from the publications listed in Section 1, and masses were estimated from Zeng et al. (2016; with an Earth-like core mass fraction of 0.33) where not available. In addition, we adopted the updated mass measurements for TRAPPIST-1 (T-1) from Grimm et al. (2018). Wherever missing from the publications listed in Section 1, J - and K_S -band fluxes were adopted from Ducati (2002) and Skrutskie et al. (2006).

overlaid on detrended and co-added MEarth and TESS data; the transit depth is consistent within 1σ in either data set, and the residual noise levels are comparable.

The mass and radius of the star are not well constrained by the time-series photometry alone and are almost entirely dictated by the prior distributions. The model finds a well-defined stellar rotation period of $P_{\text{rot}} = 17.4264 \pm 0.0094$ hr. Even though the periodicity of the rotation can be established with great precision, the photometric modulation itself has multiple peaks per rotation, pointing to a heterogeneous distribution of spots across the photosphere. The shape of the modulation imprinted onto the TESS light curve can be seen in Figure 6. However, there is no visual evidence of substantial evolution of the modulated signal over the two and a half months of data collection, facilitating the modeling necessary to isolate the transits of TOI 540 b.

The combination of a slowly evolving starspot distribution and a short orbital period that allows for the observation of a large number of transits provides a rare opportunity to make use of TOI 540 to study the atmospheric composition and escape in small planets orbiting active M dwarfs. Out of the known planet systems within 15 pc of the Sun, similar conditions may perhaps be found only in the TRAPPIST-1 system (TRAPPIST-1 has been estimated to spin with a period of 1.4 or 3.3 days; Gillon et al. 2016; Luger et al. 2017)—however, TOI 540 is nearly 2 mag brighter in the J band (and even more so toward the visible). In particular, rapidly rotating M dwarfs have more flares and coronal mass ejections, stronger stellar winds, and higher levels of X-ray and UV emission compared to slowly rotating M dwarfs, which likely lead to extensive atmospheric erosion (Vida et al. 2017; Newton et al. 2018 and references therein). Wright et al. (2018) demonstrate a clear relationship between a star’s Rossby number $\text{Ro} = P_{\text{rot}}/\tau$ (the ratio of the rotation period to the convective

turnover time) and its coronal X-ray emission as a fraction of the bolometric luminosity. For stars with $\text{Ro} > 0.14$, this relationship has a power-law slope, with smaller Rossby numbers corresponding to higher X-ray luminosities. Stars with $\text{Ro} < 0.14$ (rapid rotators) have the highest levels of X-ray emission that remains saturated at a constant level of $L_X/L_{\text{bol}} \simeq 10^{-3}$. Using an empirically calibrated relation based on the $V_J - K_S$ color, we can calculate the convective turnover time of TOI 540 to be close to $\tau = 109$ days (Wright et al. 2018, Equation (5)). This corresponds to a Rossby number of $\text{Ro} = 0.007$, suggesting that TOI 540 is in the saturated high X-ray emission regime with an X-ray-to-bolometric luminosity ratio of $L_X/L_{\text{bol}} \simeq 10^{-3}$. This hypothesis is consistent with the X-ray detection of TOI 540 by XMM-Newton that yields $L_X/L_{\text{bol}} = 0.0028$. Of the transiting planet hosts listed in Section 1, the only other star likely to be in the saturated regime is TRAPPIST-1 with $\text{Ro} \approx 0.002 - 0.006$. This is based on an estimated convective turnover time of $\tau = 582$ days that may be inaccurate as it was derived from stars with $V_J - K_S < 7.0$ (Wright et al. 2018) whereas TRAPPIST-1 is substantially redder with $V_J - K_S = 8.5$ (Gillon et al. 2017b). The bright X-ray flux of TOI 540 could present an opportunity to study transits in the X-ray to search for atmospheric loss, although we note that the atmospheric signature would likely be much smaller than the similar detection for HD 189733 b by Poppenhaeger et al. (2013).

The planet is likely to be hot: it receives 23.4 times the total radiation from its host star than Earth does from the Sun (and 3.5 times more than Mercury does), equating to a zero-albedo equilibrium temperature of $T_{\text{eq}} = 611 \pm 23$ K. The high temperature, however, may make it more amenable to transmission and emission spectroscopy measurements. We calculate the transmission spectroscopy metric (TSM) and emission spectroscopy metric (ESM) from Kempton et al.

(2018) for all of the nearby transiting terrestrial planets, listed in Section 1. The values are displayed in Figure 7. Crucially, the two best targets in the top right of Figure 7 (55 Cnc e and HD 219134 b) orbit larger K dwarfs and may not be detectable by the James Webb Space Telescope (JWST) once a systematic noise floor is taken into account. Using the scale factors from Kempton et al. (2018), we obtain $TSM = 38.9$ and $ESM = 6.8$ for TOI 540 b. The TSM value is above the threshold of 10 suggested by Kempton et al. (2018) and exceeds the TSM values of all but one of the known planets orbiting M dwarfs in Figure 7. Therefore, TOI 540 b is a prime target for transmission spectroscopy to study a potential high mean molecular weight atmosphere, if indeed such an atmosphere can be retained in close proximity to an active M dwarf. Furthermore, the relatively high ESM value will likely qualify the planet for infrared photometry with JWST to detect or rule out the presence of an atmosphere in as much as a single secondary eclipse (Koll et al. 2019). Finally, studies of the near-infrared or infrared phase curve could also tell us if TOI 540 has retained an atmosphere. A thermal phase curve study was used by Kreidberg et al. (2019) to rule out the presence of a thick atmosphere on LHS 3844 b, an ultra-short-period terrestrial planet orbiting a more evolved and less active M dwarf that has spun down to a rotation period of 128 days (Vanderspek et al. 2019) but has a mass similar to that estimated for TOI 540. A similar thermal phase curve study for TOI 540 is promising.







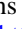



We also cannot rule out the presence of additional transiting planets in this active system. We carried out a box least-squares analysis (Kovács et al. 2002; Burke et al. 2006) as implemented in Ment et al. (2019) on the TESS light curve, but did not find sufficient evidence for additional transiting planets, consistent with the results of the SPOC’s search for additional planets. Considering the orbital inclination angle of TOI 540 b, any coplanar transiting planets would be limited to orbital periods of 1.83 days or less, which would likely lead to dynamical instability given the orbital period of TOI 540 b. Therefore, any additional planets around TOI 540 are likely to be nontransiting, or have an inclination substantially closer to 90° than TOI 540 b. Given the cumulative occurrence rate of 2.5 ± 0.2 small planets ($1-4 R_\oplus$, $P < 200$ days) per M dwarf (Dressing & Charbonneau 2015) that was derived from the Kepler population, alternative methods such as TTV (not detected for the 59 transits observed here) or RV studies (provided that enough observations can be accumulated to overcome the significant rotational broadening of spectral lines) may be fruitful to uncover more planets around TOI 540. In addition, high-resolution spectroscopy would allow for a precise modeling of line profiles during transit, yielding a direct measurement of stellar obliquity from Doppler tomography/the Rossiter–McLaughlin effect.








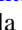



The MEarth team acknowledges funding from the David and Lucile Packard Fellowship for Science and Engineering (awarded to D.C.). This material is based on work supported by the National Science Foundation under grants AST-0807690, AST-1109468, AST-1004488 (Alan T. Waterman Award), and AST-1616624. This publication was made possible through the support of a grant from the John Templeton Foundation. The opinions expressed in this publication are those of the authors and do not necessarily reflect the views of the John Templeton Foundation. This

material is based upon work supported by the National Aeronautics and Space Administration under grant No. 80NSSC18K0476 issued through the XRP Program. A.A.M. acknowledges support from the NSF Graduate Research Fellowship under grant No. DGE1745303. R.C. is supported by a grant from the National Aeronautics and Space Administration in support of the TESS science mission. M.R. D. is supported by CONICYT-PFCHA/Doctorado Nacional-21140646, Chile. J.S.J. is supported by funding from Fondecyt through grant 1201371 and partial support from CONICYT project Basal AFB-170002. B.R.A. acknowledges the funding support from FONDECYT through grant 11181295. We acknowledge the use of public TESS Alert data from the pipelines at the TESS Science Office and at the TESS Science Processing Operations Center. Resources supporting this work were provided by the NASA High-End Computing (HEC) Program through the NASA Advanced Supercomputing (NAS) Division at Ames Research Center for the production of the SPOC data products. This research was made possible through the use of the AAVSO Photometric All-Sky Survey (APASS), funded by the Robert Martin Ayers Sciences Fund and NSF AST-1412587. This publication makes use of data products from the Two Micron All Sky Survey, which is a joint project of the University of Massachusetts and the Infrared Processing and Analysis Center/California Institute of Technology, funded by the National Aeronautics and Space Administration and the National Science Foundation. For securing the VRI photometry reported in this work, we thank RECONS (www.recons.org) members Andrew Couperus, Todd Henry, Wei-Chun Jao, and Eliot Vrijmoet. This work has made use of data from the European Space Agency (ESA) mission Gaia (<https://www.cosmos.esa.int/gaia>), processed by the Gaia Data Processing and Analysis Consortium (DPAC; <https://www.cosmos.esa.int/web/gaia/dpac/consortium>). Funding for the DPAC has been provided by national institutions, in particular the institutions participating in the Gaia Multilateral Agreement. This research has made use of data obtained from XMM-SL2, the Second XMM-Newton Slew Survey Catalogue, produced by members of the XMM SOC, the EPIC consortium, and using work carried out in the context of the EXTrAS project (“Exploring the X-ray Transient and variable Sky,” funded from the EU’s Seventh Framework Programme under grant agreement No. 607452). This research made use of exoplanet (Foreman-Mackey et al. 2019) and its dependencies (Agol et al. 2020; Astropy Collaboration et al. 2013, 2018; Foreman-Mackey et al. 2017; Foreman-Mackey 2018; Luger et al. 2019; Salvatier et al. 2016; Theano Development Team 2016).

Facilities: TESS, MEarth, CTIO:1.5 m (CHIRON), ESO:3.6 m (HARPS), SOAR, XMM.

ORCID iDs

Kristo Ment  <https://orcid.org/0000-0001-5847-9147>
 David Charbonneau  <https://orcid.org/0000-0002-9003-484X>
 Jennifer G. Winters  <https://orcid.org/0000-0001-6031-9513>
 Amber Medina  <https://orcid.org/0000-0001-8726-3134>
 Ryan Cloutier  <https://orcid.org/0000-0001-5383-9393>
 Matías R. Díaz  <https://orcid.org/0000-0002-2100-3257>
 James S. Jenkins  <https://orcid.org/0000-0003-2733-8725>
 Carl Ziegler  <https://orcid.org/0000-0002-0619-7639>
 Nicholas Law  <https://orcid.org/0000-0001-9380-6457>
 Andrew W. Mann  <https://orcid.org/0000-0003-3654-1602>

George Ricker  <https://orcid.org/0000-0003-2058-6662>
 Roland Vanderspek  <https://orcid.org/0000-0001-6763-6562>
 David W. Latham  <https://orcid.org/0000-0001-9911-7388>
 Joshua N. Winn  <https://orcid.org/0000-0002-4265-047X>
 Jon M. Jenkins  <https://orcid.org/0000-0002-4715-9460>
 Robert F. Goetze  <https://orcid.org/0000-0003-1748-5975>
 Alan M. Levine  <https://orcid.org/0000-0001-8172-0453>
 Bárbara Rojas-Ayala  <https://orcid.org/0000-0002-0149-1302>
 Pamela Rowden  <https://orcid.org/0000-0002-4829-7101>
 Eric B. Ting  <https://orcid.org/0000-0002-8219-9505>
 Joseph D. Twicken  <https://orcid.org/0000-0002-6778-7552>

References

- Agol, E., Luger, R., & Foreman-Mackey, D. 2020, *AJ*, **159**, 123
- Astropy Collaboration, Price-Whelan, A. M., Sipőcz, B. M., et al. 2018, *AJ*, **156**, 123
- Astropy Collaboration, Robitaille, T. P., Tollerud, E. J., et al. 2013, *A&A*, **558**, A33
- Baraffe, I., Chabrier, G., Allard, F., & Hauschildt, P. H. 2002, *A&A*, **382**, 563
- Batalha, N. M., Borucki, W. J., Bryson, S. T., et al. 2011, *ApJ*, **729**, 27
- Bayless, A. J., & Orosz, J. A. 2006, *ApJ*, **651**, 1155
- Benedict, G. F., Henry, T. J., Franz, O. G., et al. 2016, *AJ*, **152**, 141
- Berta-Thompson, Z. K., Irwin, J., Charbonneau, D., et al. 2015, *Natur*, **527**, 204
- Boller, T., Freyberg, M. J., Trümper, J., et al. 2016, *A&A*, **588**, A103
- Bonfils, X., Almenara, J. M., Cloutier, R., et al. 2018, *A&A*, **618**, A142
- Bouchy, F., Pepe, F., & Queloz, D. 2001, *A&A*, **374**, 733
- Boyajian, T. S., von Braun, K., van Belle, G., et al. 2012, *ApJ*, **757**, 112
- Burke, C. J., Gaudi, B. S., DePoy, D. L., & Pogge, R. W. 2006, *AJ*, **132**, 210
- Butler, R. P., Vogt, S. S., Marcy, G. W., et al. 2004, *ApJ*, **617**, 580
- Charbonneau, D., Berta, Z. K., Irwin, J., et al. 2009, *Natur*, **462**, 891
- Claret, A. 2018, *A&A*, **618**, A20
- Cloutier, R., Astudillo-Defru, N., Bonfils, X., et al. 2019, *A&A*, **629**, A111
- Cloutier, R., Eastman, J. D., Rodriguez, J. E., et al. 2020a, *AJ*, **160**, 3
- Cloutier, R., & Menou, K. 2020, *AJ*, **159**, 211
- Cloutier, R., Rodriguez, J. E., Irwin, J., et al. 2020b, *AJ*, **160**, 22
- Davenport, J. R. A. 2016, *ApJ*, **829**, 23
- Dittmann, J. A., Irwin, J. M., Charbonneau, D., et al. 2017, *Natur*, **544**, 333
- Dressing, C. D., & Charbonneau, D. 2015, *ApJ*, **807**, 45
- Dressing, C. D., Charbonneau, D., Dumusque, X., et al. 2015, *ApJ*, **800**, 135
- Ducati, J. R. 2002, *yCat*, **2237**, 0
- Finch, C. T., Zacharias, N., Subasavage, J. P., Henry, T. J., & Riedel, A. R. 2014, *AJ*, **148**, 119
- Foreman-Mackey, D. 2018, *RNAAS*, **2**, 31
- Foreman-Mackey, D., Agol, E., Ambikasaran, S., & Angus, R. 2017, *AJ*, **154**, 220
- Foreman-Mackey, D., Czekala, I., Luger, R., et al. 2019, dfm/exoplanet: exoplanet v0.2.1, Zenodo, doi:10.5281/zenodo.3462740
- Fulton, B. J., Petigura, E. A., Howard, A. W., et al. 2017, *AJ*, **154**, 109
- Gagné, J., Mamajek, E. E., Malo, L., et al. 2018, *ApJ*, **856**, 23
- Gaia Collaboration, Brown, A. G. A., Vallenari, A., et al. 2018, *A&A*, **616**, A1
- Garcia-Sage, K., Gloer, A., Drake, J. J., Gronoff, G., & Cohen, O. 2017, *ApJL*, **844**, L13
- Gillon, M., Demory, B.-O., Van Grootel, V., et al. 2017a, *NatAs*, **1**, 0056
- Gillon, M., Jehin, E., Lederer, S. M., et al. 2016, *Natur*, **533**, 221
- Gillon, M., Pont, F., Demory, B. O., et al. 2007, *A&A*, **472**, L13
- Gillon, M., TriAUD, A. H. M. J., Demory, B.-O., et al. 2017b, *Natur*, **542**, 456
- Ginzburg, S., Schlichting, H. E., & Sari, R. 2018, *MNRAS*, **476**, 759
- Goldreich, P., & Soter, S. 1966, *Icar*, **5**, 375
- Grimm, S. L., Demory, B.-O., Gillon, M., et al. 2018, *A&A*, **613**, A68
- Gronoff, G., Arras, P., Baraka, S. M., et al. 2020, *JGRA*, **25**, e27639
- Haywood, R. D., Collier Cameron, A., Queloz, D., et al. 2014, *MNRAS*, **443**, 2517
- Howard, A. W., Sanchis-Ojeda, R., Marcy, G. W., et al. 2013, *Natur*, **503**, 381
- Husser, T. O., Wende-von Berg, S., Dreizler, S., et al. 2013, *A&A*, **553**, A6
- Irwin, J. M., Berta-Thompson, Z. K., Charbonneau, D., et al. 2015, in 18th Cambridge Workshop on Cool Stars, Stellar Systems, and the Sun, ed. G. van Belle & H. C. Harris (Flagstaff, AZ: Lowell Observatory), 767
- Irwin, J. M., Charbonneau, D., Esquerdo, G. A., et al. 2018, *AJ*, **156**, 140
- Jenkins, J. M., Twicken, J. D., McCauliff, S., et al. 2016, *Proc. SPIE*, **9913**, 99133E
- Kempton, E. M. R., Bean, J. L., Louie, D. R., et al. 2018, *PASP*, **130**, 114401
- Koll, D. D. B., Malik, M., Mansfield, M., et al. 2019, *ApJ*, **886**, 140
- Kostov, V. B., Schlieder, J. E., Barclay, T., et al. 2019, *AJ*, **158**, 32
- Kovács, G., Zucker, S., & Mazeh, T. 2002, *A&A*, **391**, 369
- Kreidberg, L., Koll, D. D. B., Morley, C., et al. 2019, *Natur*, **573**, 87
- Lacy, C. H., Moffett, T. J., & Evans, D. S. 1976, *ApJS*, **30**, 85
- Lee, E. J., Chiang, E., & Ormel, C. W. 2014, *ApJ*, **797**, 95
- Leggett, S. K., Allard, F., Geballe, T. R., Hauschildt, P. H., & Schweitzer, A. 2001, *ApJ*, **548**, 908
- Li, J., Tenenbaum, P., Twicken, J. D., et al. 2019, *PASP*, **131**, 024506
- Lindgren, L., Hernández, J., Bombrun, A., et al. 2018, *A&A*, **616**, A2
- Lopez, E. D., & Fortney, J. J. 2013, *ApJ*, **776**, 2
- Lopez, E. D., & Rice, K. 2018, *MNRAS*, **479**, 5303
- Luger, R., Agol, E., Foreman-Mackey, D., et al. 2019, *AJ*, **157**, 64
- Luger, R., Sestovic, M., Kruse, E., et al. 2017, *NatAs*, **1**, 0129
- Luque, R., Pallé, E., Kossakowski, D., et al. 2019, *A&A*, **628**, A39
- Mamajek, E. E. 2012, *ApJL*, **754**, L20
- Mann, A. W., Feiden, G. A., Gaidos, E., Boyajian, T., & von Braun, K. 2015, *ApJ*, **804**, 64
- Mayor, M., Pepe, F., Queloz, D., et al. 2003, *Msngr*, **114**, 20
- McArthur, B. E., Endl, M., Cochran, W. D., et al. 2004, *ApJL*, **614**, L81
- Medina, A. A., Winters, J. G., Irwin, J. M., & Charbonneau, D. 2020, arXiv:2010.15635
- Ment, K., Dittmann, J. A., Astudillo-Defru, N., et al. 2019, *AJ*, **157**, 32
- Morley, C. V., Kreidberg, L., Rustamkulov, Z., Robinson, T., & Fortney, J. J. 2017, *ApJ*, **850**, 121
- Motalebi, F., Udry, S., Gillon, M., et al. 2015, *A&A*, **584**, A72
- Newton, E. R., Irwin, J., Charbonneau, D., et al. 2016, *ApJ*, **821**, 93
- Newton, E. R., Mondrik, N., Irwin, J., Winters, J. G., & Charbonneau, D. 2018, *AJ*, **156**, 217
- Nutzman, P., & Charbonneau, D. 2008, *PASP*, **120**, 317
- Owen, J. E., & Wu, Y. 2013, *ApJ*, **775**, 105
- Owen, J. E., & Wu, Y. 2017, *ApJ*, **847**, 29
- Pecaut, M. J., & Mamajek, E. E. 2013, *ApJS*, **208**, 9
- Pepe, F., Cameron, A. C., Latham, D. W., et al. 2013, *Natur*, **503**, 377
- Poppenhaeger, K., Schmitt, J. H. M. M., & Wolk, S. J. 2013, *ApJ*, **773**, 62
- Ricker, G. R., Winn, J. N., Vanderspek, R., et al. 2015, *JATIS*, **1**, 014003
- Rogers, L. A. 2015, *ApJ*, **801**, 41
- Salvatier, J., Wiecki, T. V., & Fonnesbeck, C. 2016, *PeerJ Computer Science*, **2**, e55
- Skrutskie, M. F., Cutri, R. M., Stiening, R., et al. 2006, *AJ*, **131**, 1163
- Skumanich, A. 1972, *ApJ*, **171**, 565
- Smith, J. C., Stumpe, M. C., Van Cleve, J. E., et al. 2012, *PASP*, **124**, 1000
- Soto, M. G., Díaz, M. R., Jenkins, J. S., et al. 2018, *MNRAS*, **478**, 5356
- Stassun, K. G., Oelkers, R. J., Pepper, J., et al. 2018, *AJ*, **156**, 102
- Stumpe, M. C., Smith, J. C., Catanzarite, J. H., et al. 2014, *PASP*, **126**, 100
- Stumpe, M. C., Smith, J. C., Van Cleve, J. E., et al. 2012, *PASP*, **124**, 985
- Theano Development Team 2016, arXiv:1605.02688
- Tokovinin, A. 2018, *PASP*, **130**, 035002
- Tokovinin, A., Fischer, D. A., Bonati, M., et al. 2013, *PASP*, **125**, 1336
- Twicken, J. D., Catanzarite, J. H., Clarke, B. D., et al. 2018, *PASP*, **130**, 064502
- Vanderspek, R., Huang, C. X., Vanderburg, A., et al. 2019, *ApJL*, **871**, L24
- Vida, K., Kővári, Z., Pál, A., Oláh, K., & Kriskovics, L. 2017, *ApJ*, **841**, 124
- Vogt, S. S., Burt, J., Meschiari, S., et al. 2015, *ApJ*, **814**, 12
- Weiss, L. M., & Marcy, G. W. 2014, *ApJL*, **783**, L6
- Winn, J. N., Matthews, J. M., Dawson, R. I., et al. 2011, *ApJL*, **737**, L18
- Winters, J. G., Irwin, J. M., Charbonneau, D., et al. 2020, *AJ*, **159**, 290
- Winters, J. G., Medina, A. A., Irwin, J. M., et al. 2019, *AJ*, **158**, 152
- Wright, N. J., Newton, E. R., Williams, P. K. G., Drake, J. J., & Yadav, R. K. 2018, *MNRAS*, **479**, 2351
- Zeng, L., Sasselov, D. D., & Jacobsen, S. B. 2016, *ApJ*, **819**, 127
- Ziegler, C., Tokovinin, A., Bricño, C., et al. 2020, *AJ*, **159**, 19